

Remote Focusing

An Exploration of Theory and Application to Microscopy

Alexander Marshall*
Optics 515

May 1, 2024

Contents

1	Theory of Remote Focusing	ii
1.1	Introduction	ii
1.2	Fourier Optics Approach	ii
1.3	Ray Optics Approach	iii
2	Remote Focusing Example	iv
2.1	Introduction to Optical System	iv
2.2	Predictions	iv
2.3	ETL Calibration	v
2.4	Light-Sheet Characterization	v
3	Results and Discussion	vi
3.1	ETL Calibration Results	vi
3.2	Light Sheet Characterization	vi
3.3	Discussion	vi
	References	ix

*The University Of North Carolina Department of Physics and Astronomy

1 Theory of Remote Focusing

1.1 Introduction

In microscopy, high-NA objectives are often associated with very narrow depth of focus, which in biological imaging is frequently much thinner than the region of interest in a given sample. One way to address this is to mechanically translate the objective (or sample) along the optical axis, thus moving the focal plane along with it. However, this process tends to be slow and difficult to integrate with other systems control, and in the case of fluorescence microscopy fails to decouple the excitation focal plane from the detection focal plane. Furthermore, the effective range of this adjustment is limited by the physical constraints of the stage and objective. If there were a way to adjust the focal plane without physically moving the objective or better yet without relying on mechanical translations at all, this would allow for far more rapid volumetric imaging.

Remote focusing is a way to optically translate the focal plane of an objective without directly moving it. While there are other approaches to remote focusing [1], in our lab we use tunable lenses conjugate to the back focal plane of the objective to achieve this without the physical translation of components. [2] This allows for rapidly adjusting the focal plane large distances within milliseconds, which has exciting applications in biological imaging. [3] Introducing minimal aberration and magnification, it is an exciting tool which allows fast, automated three dimensional imaging. There are a diverse array of types of electronically tunable lenses, or ETLs. Our system uses Optotune electronically tunable lenses, which pass a user-specified current through a hydraulically-shaped meniscus, causing electromagnetic activation of the fluid. This causes a change in the fluid lens volume, altering the dioptric power of the lens. [4] In our lab, we also use remote focusing in the excitation light-path to dynamically control the focal plane of our illumination beam, enabling advanced techniques such as total internal reflection or highly inclined swept tile fluorescence microscopy. To understand the theory behind this technique, I

summarize the derivation of remote focusing via Fourier Optics, then analyze its behavior using geometric optics.

1.2 Fourier Optics Approach

This section closely follows the derivation performed by Zuo et al. [5] We start off with assuming our system is telemetric, which in this case means that refocusing avoids the introduction of additional phase-curvature across the field of view. This would result in the addition of variable magnification across the field of view. This is crucial, as otherwise data processing would be unduly arduous and under this assumption, we can model the propagation of the wavefunction u_0 modified by the free space transfer function H as follows.

$$u_{\Delta z}(x, y) = \mathcal{F}^{-1} [\mathcal{F}(u_0(x, y)) H_{\Delta z}(u, v)] \quad (1)$$

In brackets, we see that we have taken the Fourier transform of the wave to find its corresponding frequency-space function, and then modify that with the transfer function. In the paraxial approximation the free space transfer function is known to be

$$H_{\Delta z}(u, v) = \exp [-i\pi\lambda\Delta z(u^2 + v^2)]. \quad (2)$$

Replicating the phase modification of free space via a spatial light modulator (SLM) represents the angular spectrum method and is widely used in holographic reconstruction due to its ability to produce an image field which does not vary in size along the optical axis. However, there are many practical difficulties of working with an SLM, so we instead utilize an electronically tunable lens (ETL). In Fourier optics, in the paraxial approximation a lens produces a transfer function of the form [6]

$$t_l(x, y) = \exp \left[-i \frac{k}{2f} (x^2 + y^2) \right]. \quad (3)$$

Since our ETL is in the spatial coordinates of the Fourier plane of the 4f system, it has a transfer function

$$t_l(\xi, \eta) = \exp \left[\frac{-i\pi}{\lambda f_c} (\xi^2 + \eta^2) \right]. \quad (4)$$

Notice that equation 4 is similar in form to the free space transfer function given in equation (2);

by selecting a specific combined focal length f_c , we can do the equivalent of propagating the wave through free space some distance Δz . In our case, we use only a stand-alone ETL rather than a combined system, so $f_c = f_e$. Converting from spatial to frequency coordinates in the Fourier plane, we can compare it to our known free space transfer function $H_{\Delta z}$ above and solve for axial translation as a function of the tunable focal length.

$$H_{\Delta z}(u, \nu) = t_l(\xi, \eta) \quad (5)$$

$$\exp[-i\pi\lambda\Delta z(u^2 + \nu^2)] = \exp\left[\frac{-i\pi}{\lambda f_e}((\lambda f u)^2 + (\lambda f \nu)^2)\right] \quad (6)$$

$$\Delta z = \frac{f^2}{f_e} \quad (7)$$

1.3 Ray Optics Approach

In this section, we follow the derivation performed by Qu and Hu. [7] When centered at the focal plane of two relay lenses rather than at the back focal plane, ETL3 also causes minor demagnification at high dioptric power. To see why this is, we turn to another paper which analyzes the impact of a remote focusing objective in the detection pathway in more detail. We begin with the thin lens equation

$$\frac{1}{I} + \frac{1}{I'} = \frac{1}{f'_O} \quad (8)$$

for f'_O is the focal length of the objective, I is the distance between the object and the objective and I' is the distance between the objective and the image. Now let us assume that we have an ETL at the back focal plane of our objective. This ETL produces an axial translation of the focal plane Δz . This means we may now write a system of two thin lens equations to model the light going from the object plane, through the objective, to the BFP where the ETL is, and then to the imaging plane.

$$\frac{1}{I - \Delta z} + \frac{1}{I'_1} = \frac{1}{f} \quad (9)$$

$$\frac{1}{f - I'_1} + \frac{1}{I'_2} = \frac{1}{f'_e} \quad (10)$$

The first thin lens equation models the system from the new object plane, which has been shifted by Δz from the old object plane via remote focusing by the ETL, through the objective, and to the image after the objective at a distance of I'_1 . The second thin lens equation models the system from the image after the objective through the ETL of variable focal length f_e and to the second image after the ETL at a distance of I'_2 . Due to the configuration of our system, the distance between the image after the objective and the objective is equal to the distance from the objective to the ETL at the back focal plane, which is the focal length, and the distance from ETL2 to the image after ETL2 where the camera is placed, so that

$$I' = I'_2 + f'_O. \quad (11)$$

Now, we solve the system of equations given by 8-11 via MATLAB ¹ to find Δz .

$$\Delta z = \frac{f^2}{f'_e} \quad (12)$$

This result is similar to the result we got in equation 7, but here our objective is in the back focal plane of the system and f is the objective's focal length, which is related to the magnification of our system.

Let us pivot to considering a 4F system with two relay lenses and an ETL in the plane conjugate to the back focal plane. In our system, ETL2 and ETL3 are at the focal plane of two relay lenses conjugate to the back focal plane rather than in the back focal plane itself, so this will model a system analogous to ours. In this case, we get thin lens equations describing the transition from object through the objective to the image and from the intermediate image through the ETL to the detector

$$\frac{1}{I - \Delta z} + \frac{1}{I'_1} = \frac{1}{f} \quad (13)$$

$$\frac{1}{I' + f'_r - I'_1} + \frac{1}{I'_2} = \frac{1}{f'_r} \quad (14)$$

where we maintain the same variable convention and introduce I'_2 is the distance between the image after the first relay lens and the relay lens

¹Code available upon request

and f'_r is the focal length of the relay lenses. In this system, since the ETL is a distance d_1 from the relay lens, we get

$$d_1 = I'_2 + f'_e. \quad (15)$$

The distance from the relay lens to the ETL is given by

$$d_1 = f'_r + \frac{f'^2_2}{M'_O f}. \quad (16)$$

Using MATLAB, we solve for Δz

$$\Delta z = \frac{f'^2_r}{M'^2_O f'_e} \quad (17)$$

where $M'_O = (f'_O - I)/f'_O$ is the magnification of our system. We must also account for the fact that in our system, our ETLs are always in air so $n \approx 1$ while the objective is in an immersion media with some index n . Accommodating this [8] gives us our final expression for axial translation in an immersion media.

$$\Delta z = \frac{n f'^2_r}{M'^2_O f'_e}. \quad (18)$$

While this configuration allows much less translation range than the back focal plane setup, it offers key advantages. Theoretically, the dioptric power of the ETL does not affect the magnification of the system in either the back focal plane or conjugate to the back focal plane. However, in practice it causes both demagnification and irregular spatial distortions in the image. While these issues are quite pronounced in the back focal plane setup, they are more limited in the relay lens setup and are negligible under low dioptric power. [7][8] Furthermore, the relay lens setup allows us to use two relay lenses in a fluorescent light microscopy setup, with one to translate the excitation pathway and the other to translate the emission pathway.

2 Remote Focusing Example

2.1 Introduction to Optical System

Our optical system [2][9] (see Figure 1) is designed for light sheet fluorescence microscopy, and has two paths which diverge at the dichroic

mirror of a filter cube just after a shared objective. In our system, we have three identical electrically tunable lenses (Optotune, EL-10-40-TC-VIS-20D), two of which are used for remote focusing. [2] We control ETLs by passing a known current through each via a controller box (Optotune, ICC-4C) which is in turn controlled by custom LabVIEW software and Optotune Cockpit. The first, ETL 2, is responsible for remote focusing in the illumination light path, while the second, ETL3, is responsible for focusing in the detection light path. In our field of research, it is important to be able to translate the focal plane of the light sheet by a set amount using ETL2, while ETL3 must be able to move the imaging plane to the same location. In order to use these devices as designed, we must therefore create a look up-table for each ETL, tying applied current to optical axis translation Δz .

2.2 Predictions

In theory, the current $I \propto P_e$, where P_e is the dioptric power of the lens $P_e = 1/f_e$. Defining $\Delta P_e \equiv P_{e-max} - P_{e-min}$, we can rewrite eq. 18 in terms of dioptric power for a more convenient form expressed as

$$\Delta z = \frac{n \Delta P_e f'^2_r}{M'^2_O}. \quad (19)$$

For our predictions, we assume each ETL has the manufacturer-guaranteed dioptric power range of $P \in [-10, 10]m^{-1}$ diopters, so $\Delta P_e = 20m^{-1}$. In practice, the dioptric powers of these lenses likely exceed these parameters, and the actual relationship between current and lens focal power is dependent on component temperature, but is highly replicable under relatively consistent lab conditions.

In theory, both the remote focusing ETLs follow equation 19. Since we have $f = 125mm$ relay lenses [9], we get a predicted axial transfer range of $\Delta z = 15625mm^2 P_e / M'^2_O$. This predicts a range of $\pm 591\mu m$ for a 20X objective and $\pm 66\mu m$ for a 60X objective. However, we may control only current applied to the ETL, which controls dioptric power. Dioptric power is dependent on both current and lens temperature. The non-ideal behavior of the ETL compounds with

the non-ideal behavior of optics so that in practice, experimental behavior differs significantly from theoretical predictions. To ensure accurate axial control, we calibrate our ETLs under anticipated experimental conditions.

Going forward, it will be important to differentiate between the excitation focal plane, the sample plane, and the detection focal plane. The *excitation* focal plane is the plane in which the beam waist lies, and is translated via altering the dioptric power of ETL2 or physically moving the objective. The sample plane is the physical location of the sample's surface, and is static for any given experiment. The *detection* focal plane is the plane which is imaged on the CCD, and is translated via altering the dioptric power of ETL3 or physically moving the objective.

2.3 ETL Calibration

ETL2 is in the excitation pathway of our system. Using a light sheet, we will first focus the excitation beam into the sample plane via objective height adjustment and ETL2. We use a slide coated generously with fluorescent 200nm beads as our sample.

We use μ Manager[10] to move the microscope objective upwards in the Z direction in known discrete steps. We then bring this image into focus in the camera via ETL3 to adjust for the objective displacement and refocus the image. We then minimize the width of a Gaussian light-sheet by using ETL2 to translate the excitation focal plane back into the sample plane. Because we are compensating for a known displacement of the objective via ETL2, we can link the current value of ETL to focal-plane translation. Taking many of these steps allows us to map the relationship between ETL2 current and Δz_{ex} . So according to Equation 19, we predict maximum axial scanning range of $\Delta z = 1183nm$ over the full theoretical dioptric range.

ETL3 is in the detection plane of the microscope. To calibrate it, we follow much the same procedure we did for ETL2, but rather than involving the excitation pathway we simplify things using the built-in transmission illumination lamp and a calibration grid, allowing us to isolate the detection pathway. As before,

we translate the objective by a known step, then compensating for the output with ETL3, moving the detection focal plane back into the sample plane and recording the current necessary to do so. In this way we can create a map of the relationship between ETL3 current and Δz_{em} .

2.4 Light-Sheet Characterization

In this experiment, we use our ETLs to decouple the emission and excitation focal planes and use this image and characterize the profile of a light sheet. First, we use ETL2 to focus the light sheet in the sample plane, where we again use a slide with 200nm beads for our sample. Then we displace the objective by known increments, translating both the emission and excitation focal planes by Δz . Then we bring the beads back into focus using ETL3, moving the emission focal plane back into the sample plane. We then image the beam at some distance from its beam waist ΔZ . After doing this for a variety of objective displacements, we analyze the images to determine the beam waist as a function of axial displacement, $\omega(z)$.

We make several predictions about the light sheet. The beam waist in a LSFM system is given by [11]

$$\omega_0 \approx \frac{0.85\lambda}{2NA} \quad (20)$$

where NA is the numerical of the illumination objective and λ is the excitation wavelength. Now, we must compute the ideal beam width and compare this with our own findings. For our 60X objective, which has an NA of 1.5, and 561nm laser excitation light, we get $\omega_0 \approx 165nm$. A beam simulator specifically designed for this purpose [12] verifies this result. This predicts a Full-Width at Half Max of $193\mu m$. For an approximately Gaussian light sheet, the Rayleigh length is

$$Z_R = \frac{\pi\omega_0^2}{\lambda} \quad (21)$$

so we should expect a Rayleigh length of around 152nm. To process my data, I used FIJI [13] to rotate my image until the light sheets were vertical in the image and created a histogram of

intensities by column. Then I added offset Gaussian fits to each plot and exported the data.

3 Results and Discussion

3.1 ETL Calibration Results

To analyze the results, we put the focal plane position to ETL current pairings into Excel and graphed them. We then created a linear best fit function for each, then extrapolated the maximum value for -10 to 10 diopters, then computed the difference between these two values to find the maximum ΔZ . For a 60X objective ETL2, we got $108\mu m$ ΔZ range. For ETL3, we get $166.6\mu m$, which is somewhat larger than anticipated. This is not really surprising; Optotune lenses are designed to exceed their rated dioptric power by some margin under most conditions.

Using the 20X objective, we obtained a scanning range of $1065\mu m$ for ETL3. This is again somewhat less than the predicted axial range, but is approximately 9 times the 60X scanning range, as predicted by equation 19.

3.2 Light Sheet Characterization

Our beam waist minimized at $0.5\mu m$ according to raw data and at $0.7\mu m$ for the Gaussian best fit curve. I found the Rayleigh length $Z_R \approx 2\mu m$. Note that this value has a lot of error in it, as our stage is able to move in only $1\mu m$ increments, so our resolution is quite limited here. Our light sheet width is a factor of around three (raw intensity profile) to five (gaussian fit) times thicker at the beam waist than anticipated. The Rayleigh length for a beam of this width is predicted to be $1.4\mu m$ and $2.74\mu m$ for $\omega_0 \approx 0.5\mu m$ and $0.7\mu m$ respectively. Thus, while our beam waist was significantly larger than predicted for our theoretical beam, our Rayleigh length was close to the predicted value for a sheet of the observed width.

3.3 Discussion

The entire Hestia system remains under active development, as is known to currently have alignment imperfections. This may be causing

some of the irregularities in ETL performance. Currently, there is no implementation of an algorithmic autofocus function implemented for either ETL, so each of these calibrations was performed using a protocol utilizing human judgement, and there was some variability in the assignment of ideal current levels, even for identical objective positions. This manual process was time consuming, limiting the amount of data acquired. At some point, we hope to develop a more standardized method for this which leads to more replicable data and less noise.

Additionally, the light sheet characterization was not conducted using advanced image deconvolution or analysis. The beads used for this sample were $200nm$ in diameter, which is large compared to the theoretical beam waist as well as potentially causing scattering. All of these factors probably contributed to a larger-than-predicted beam waist measurement and in the future, more advanced data analysis techniques using MATLAB, image deconvolution using point spread functions, and $40nm$ beads will be implemented to improve precision.

Overall, the remote focusing system performed quite close to expectations, and appeared highly linear and predictable proximal to $0mA$. Since we plan to use this system to image macrophages, a depth of $10\mu m$ of axial scanning range is sufficient for our application. The calibration curves are very linear near equilibrium, and so this will likely perform well for our application.

It should also be noted that the beam shifts a lot as ETL2 is adjusted. This indicates that there is a lot of tilt in the light sheet, i.e. the excitation beam is not parallel with the primary optical axis, and is therefore not perpendicular to the imaging plane. This is surely increasing the apparent width of the beam and likely changes the behavior of the remote focusing as well. The emission pathway is likely not tilted in the same way, so this may be one reason for the difference in ETL2 and ETL3 performance.

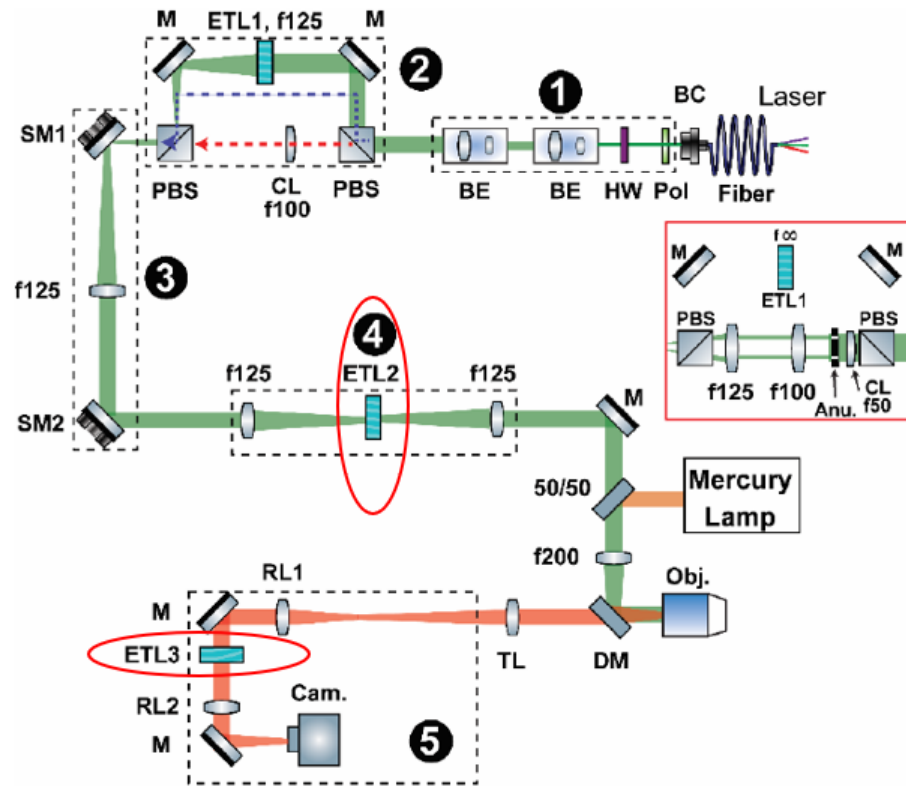


Figure 1: This figure, adapted from Liu et al [9] with the permission of the corresponding author, depicts the optical design of our system. The ETLs used for remote focusing (circled in red) are at the focal planes of the 4F system, which are conjugate to the back focal plane of the objective.

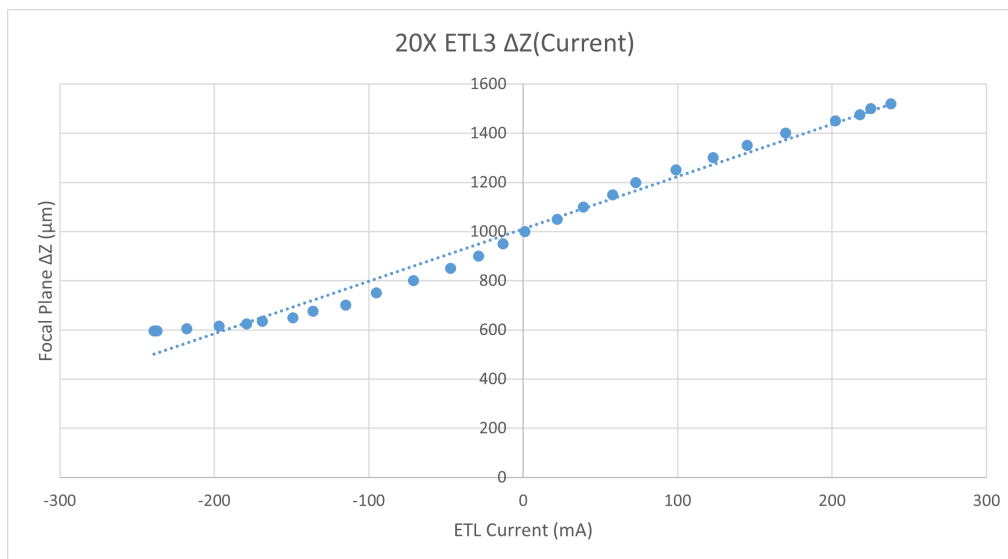


Figure 2: This graph depicts the relationship between ETL3 current and absolute focal plane position. Note the significant breakdown of linearity at large negative currents corresponds to major demagnification and spatial distortion of the image.

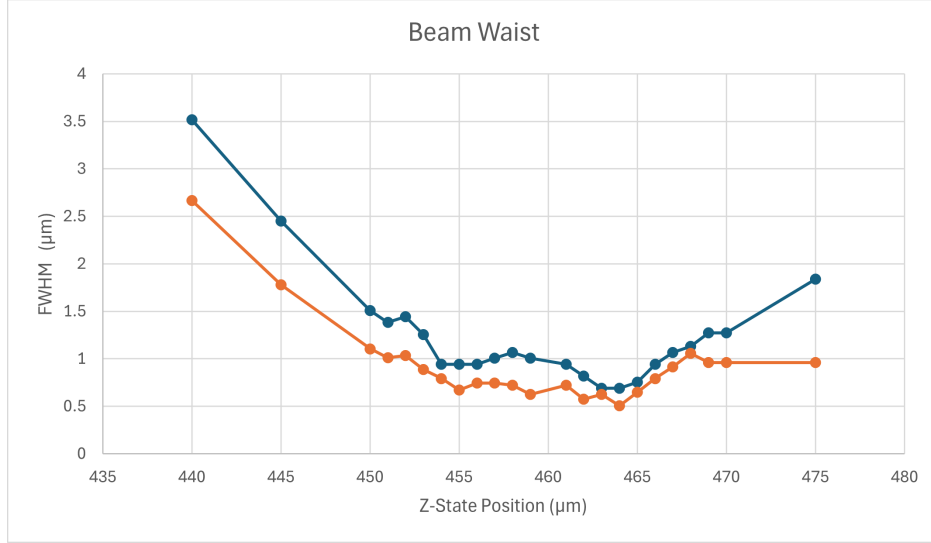


Figure 3: This graph depicts the beam waist at a given objective position. The objective used is a 60X Olympus objective. ETL3 was used to keep the beads in focus via remote focusing, allowing us to profile the beam. The red line is the FWHM according to the raw data, while the blue line shows the FWHM of a Gaussian best fit of the data.

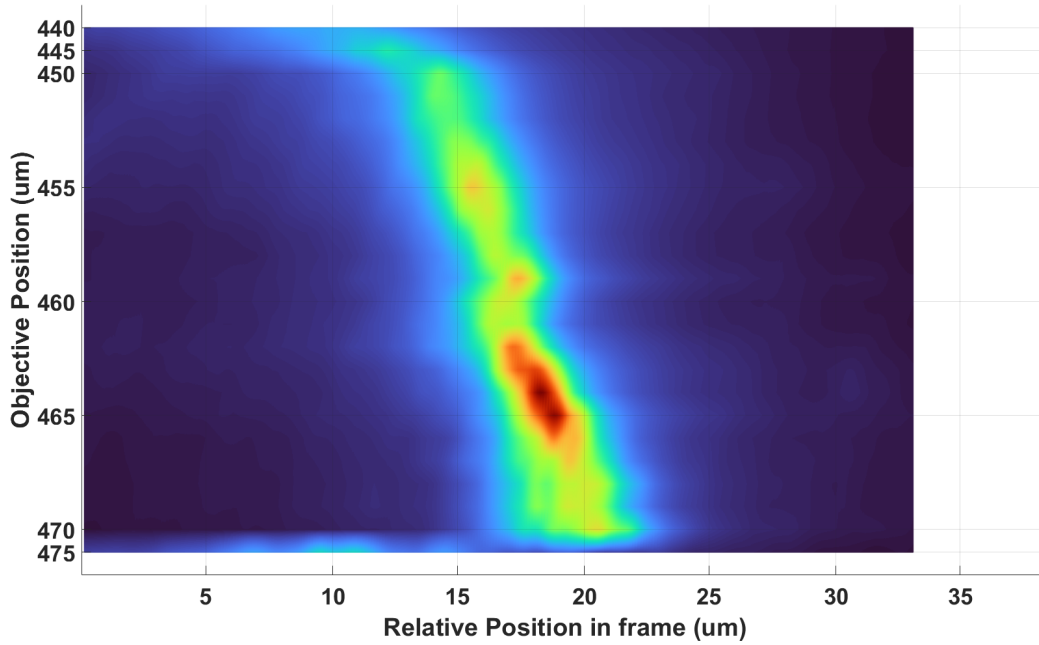


Figure 4: This heatmap displays the intensity of the light sheet as a function of objective's position. Note how the sheet tapers in width and spikes in intensity around the focal plane of the light sheet circa objective position 464 microns. The drift of the light sheet as the objective is translated upwards (down on the graph) shows the lightsheet is emerging at around 75° , rather than orthogonal to, the sample plane.

References

- [1] T. Wilson, M. Booth, R. Juskaitis, and E. Botcherby, “An optical technique for remote focusing in microscopy,” *Optics Communications*, pp. 880–887, 2007. DOI: doi:10.1016/j.optcom.2007.10.007.
- [2] C. M. Hobson, “On the biomechanics of cell nuclei: Insights from combined force and light microscopy,” Thesis, 2021.
- [3] P. Annibale and E. Dvornikov Alexander Gratton, “Electronically tunable lens speeds up 3d orbital tracking,” *Biomedical Optics Express*, vol. 6, pp. 2181–2190, 2015. DOI: DOI:10.1364/BOE.6.002181.
- [4] L. Chen, M. Ghilardi, J. J. Busfield, and F. Carpi, “Electronically tunable lenses: A review,” *Frontiers in robotics and AI*, vol. 8, pp. 1–20, 2021. DOI: doi:10.3389/frobt.2021.678046.
- [5] C. Zuo, C. Qian, and A. Weijuan Qu Asundi, “High-speed transport-of-intensity phase microscopy with an electrically tunable lens,” *OPTICS EXPRESS*, vol. 21, no. 20, 2013. DOI: DOI:10.1364/OE.21.024060.
- [6] J. W. Goodman, *Introduction to Fourier Optics, 3rd Ed.* Englewood, Colorado: Roberts and Co., 2005, ISBN: 0974707724.
- [7] Y. Qu and Y. Hu, “Analysis of axial scanning range and magnification variation in wide-field microscope for measurement using an electrically tunable lens,” *Wiley Microscopy Reserach and Technique*, vol. 82, pp. 101–113, 2019. DOI: 10.1002/jemt.23113.
- [8] F. O. Fahrbach, F. F. Voigt, B. Schmid, F. Helmchen, and J. Huisken, “Rapid 3d light-sheet microscopy with a tunable lens,” *Optics Express*, vol. 21, no. 192746, pp. 21 010–21 026, 2013. DOI: DOI:10.1364/OE.21.021010.
- [9] B. Liu, C. M. Hobson, F. M. Pimenta, *et al.*, “View-mod: A versatile illumination engine with a modular optical design for fluorescence microscopy,” *Optics Express*, vol. 27, pp. 19 950–19 972, 2019. DOI: <https://doi.org/10.1364/OE.27.019950>.
- [10] A. Edelstein, A. Nenad, K. Hoover, R. Vale, and N. Stuurman, “Computer control of microscopes using umanager,” *Current Protocols in Molecular Biology*, vol. 92, no. 1, pp. 1–17, 2010.
- [11] H. S. Ernst, F. Strobl, B.-J. Chang, *et al.*, “Light sheet fluorescence microscopy,” *Nature Reviews*, vol. 1, pp. 1–25, 2021.
- [12] E. Remacha, L. Friedrich, J. Vermot, and F. O. Fahrbach, “How to define and optimize axial resolution in light-sheet microscopy: A simulation-based approach,” *Biomedical Optics Express*, vol. 11, pp. 8–26, 2020. DOI: <https://doi.org/10.1364/BOE.11.000008>.
- [13] J. Schindelin, I. Arganda-Carreras, E. Frise, *et al.*, “Fiji: An open-source platform for biological image analysis,” *Nature Methods*, vol. 9, pp. 676–682, 2012. DOI: <https://doi.org/10.1038/nmeth.2019>.